This is a repository copy of *Tomographic eigenstrain reconstruction for full-field residual stress analysis in large scale additive manufacturing parts*.

White Rose Research Online URL for this paper:
https://eprints.whiterose.ac.uk/222212/

Version: Published Version

Article:
Uzun, F. orcid.org/0000-0002-6637-6479, Basoalto, H., Liogas, K. orcid.org/0000-0002-0620-5483 et al. (7 more authors) (2024) Tomographic eigenstrain reconstruction for full-field residual stress analysis in large scale additive manufacturing parts. Additive Manufacturing, 81. 104027. ISSN 2214-8604

https://doi.org/10.1016/j.addma.2024.104027

Reuse
This article is distributed under the terms of the Creative Commons Attribution (CC BY) licence. This licence allows you to distribute, remix, tweak, and build upon the work, even commercially, as long as you credit the authors for the original work. More information and the full terms of the licence here:
https://creativecommons.org/licenses/

Takedown
If you consider content in White Rose Research Online to be in breach of UK law, please notify us by emailing eprints@whiterose.ac.uk including the URL of the record and the reason for the withdrawal request.

eprints@whiterose.ac.uk
https://eprints.whiterose.ac.uk/

Additive Manufacturing 81 (2024) 104027

Contents lists available at ScienceDirect

Additive Manufacturing

journal homepage: www.elsevier.com/locate/addma

Tomographic eigenstrain reconstruction for full-field residual stress analysis in large scale additive manufacturing parts

Fatih Uzun [a,*], Hector Basoalto [b], Konstantinos Liogas [a], Mohamed Fares Slim [c], Tung Lik Lee [d], Cyril Besnard [a], Zifan Ivan Wang [e], Jingwei Chen [a], Igor P. Dolbnya [f], Alexander M. Korsunsky [a,*]

[a] MBLEM, University of Oxford, Department of Engineering Science, Oxford, UK
[b] University of Sheffield, Department of Materials Science and Engineering, Sheffield, UK
[c] Arts et Métiers Institute of Technology, MSMP, HESAM Université, F-13617 Aix-en-Provence, France
[d] ISIS Neutron and Muon Source, STFC Rutherford Appleton Laboratory, Harwell Campus, Didcot, Oxfordshire, UK
[e] University of Cambridge, Department of Engineering, Cambridge, UK
[f] Diamond Light Source, B16 Synchrotron Beamline, Didcot, UK

ARTICLE INFO

Keywords:
Eigenstrain reconstruction
Inherent strain
Residual stress
Diffraction strain tomography
Discontinuous processing

ABSTRACT

Current experimental and numerical quantification methods are limited in their ability to full-field mapping of the unpredictable distribution of all residual stress and permanent plastic strain components in additive manufacturing parts with discontinuous processing properties. To address this limitation, a tomographic eigenstrain (inherent strain) reconstruction method, that merges eigenstrain reconstruction with diffraction strain tomography for mapping volumetric distribution of all components of eigenstrains and corresponding elastic deformations like residual stresses non-destructively using minimum amount of tomographic scans is presented through numerical experiments, and then applied to the analysis of a CM 247 LC superalloy additive manufacturing part using diffraction strain tomography data. The method reconstructs all eigenstrain and corresponding residual stress components, parallel to the build direction, aligned with the experimental data component accurately, demonstrating its potential in optimizing the performance and reliability of parts designed for high-tech industries such as aerospace. Subsequent validations using the X-ray diffraction $\sin^2\psi$ and neutron diffraction strain scanning techniques confirm the method's reliability in reconstructing residual stress components parallel to the plane of powder bed that are different from the experimental data component. Furthermore, the novel findings of this study reveal a characteristic residual stress distribution pattern within additive manufacturing parts particularly those featuring rectangular shapes. Microstructural analysis also validates eigenstrain distribution in accordance with the findings on the characteristic distribution of residual stresses, highlighting the significance of this method in advancing materials research and development.

1. Introduction

Nickel-based alloys, including CM 247 LC superalloys, find extensive use in the aerospace industry [1–3] due to their exceptional properties like creep resistance, strength, and toughness under extreme conditions. However, their high γ'-phase content poses challenges for conventional machining [4], making additive manufacturing methods like laser powder bed fusion (LPBF) increasingly essential [5]. CM 247 LC, derived from MAR M 247 superalloy, is optimized for single crystal casting applications [6], but faces challenges such as boundary cracking during directional solidification [7] and hot cracking tendencies [8]. Weldability depends on the γ'-phase volume fraction, with alloys containing over 4.5 wt% Al and Ti being less weldable [9]. LPFB processes can induce microcracking in nickel alloys with high Al and Ti content [10–12], necessitating strategies like fractal scan patterns and pulsed wave laser deposition [13,14]. The complex thermal history during PBF manufacturing results in residual stresses, making their analysis challenging [15,16]. Minimizing these stresses is crucial to prevent cracking in aerospace parts [17,18], but this is a complex task, especially in the unpredictable conditions of laser-based additive manufacturing techniques [13].

The production of large-scale parts using LPBF often faces significant

* Corresponding authors.
E-mail addresses: fatihuzun@me.com, fatih.uzun@eng.ox.ac.uk (F. Uzun), alexander.korsunsky@eng.ox.ac.uk (A.M. Korsunsky).

https://doi.org/10.1016/j.addma.2024.104027
Received 29 October 2023; Received in revised form 2 February 2024; Accepted 4 February 2024
Available online 7 February 2024
2214-8604/© 2024 The Author(s). Published by Elsevier B.V. This is an open access article under the CC BY license (http://creativecommons.org/licenses/by/4.0/).

challenges [19]. The extended production time inherent in this process tends to introduce issues such as cracks, distortions, and overheating problems. Specifically, when employing LPBF for the fabrication of massive components made of metal alloys, the rapid solidification gives rise to irregular distribution of permanent plastic strains. These strains, in turn, cause the formation of residual stresses that have a high influence on failures such as stress corrosion cracking and fracture. Accordingly, understanding the distribution of these residuals is crucial for optimizing process parameters [20] in order to minimize failures related to these residuals.

Residual stresses formed during the widely used thermo-mechanical manufacturing processes such as welding [21,22] and additive manufacturing [23] create weak spots that are prone to crack formation and fracture while shot peening [24] forms surfaces with improved resistance to these failures. The parameters of these processes and other processes prone to the formation of residual stresses should be adjusted in a way to minimise or maximise residual stress mitigation in order to satisfy operational requirements. Accordingly, residual stresses should be quantified and analysed using experimental [25,26], numerical [27–31], and hybrid [32–35], that combine experimental data with numerical models, methods. Process simulations and in-situ experiments contribute to understanding the mechanisms leading to the formation of porosities [36] and spattering behaviour [37], which influence the development of residual stresses. However, to optimize process parameters and minimize the occurrence of such issues, a comprehensive understanding of the residual stresses in the final products is essential.

The literature has abundant number of examples of quantitative analysis of residual stresses for various processing conditions, but operational difficulties and high cost of experimentations limits the attempts on full-field mapping for both research and industrial purposes. Correlation of physical characteristics of materials with residual elastic strains are widely used to create line profiles in and around the hot spots where distribution of permanent plastic strains is expected to be irregular. These short-range one-dimensional maps provide a limited understanding the influence of processing conditions on the formation of residual stresses. Increasing the number of measurements have a potential to provide a two- or three-dimensional map of diverse measurement but labour and instrumental costs along with operational difficulties prevents applicability of these approaches. Recent advances in the creation of surface profilometry data with micro-scale sensitivity and high spatial resolution allowed the determination of displacements due to changes in boundary conditions that are created by the help of non-contact electric discharge machining [38,39]. In the case of availability of information about physical changes in large planes it has been possible to perform two-dimensional low-cost mapping of residual stresses. The contour method developed for this purpose has been extended to reconstruction of multi-axial residual stresses in continuously processed bodies using eigenstrain theory [40,41]. Improvements in the formulation of the inverse problem of eigenstrain by the help of guiding functions [42] and the implementation of principles of artificial intelligence allowed mapping the residual stresses in parts undergoing discontinuous processing [43] even after further processing like heat treatment [44]. However, the dependence on the guiding functions is preventing to understand the complex distribution of residual stresses in additive manufacturing parts. The introduction of the voxel-based full-field eigenstrain reconstruction method by Uzun and Korsunsky [45] provided new insights for the full field mapping of residual stresses. This method was validated by the reconstruction of well-known distribution of residual stresses in a bent titanium alloy using highly reliable X-ray diffraction measurements and allowed volumetric three-dimensional mapping of both eigenstrains and residual stresses accurately in the case of availability of experimental data from a limited section of a material. The use of experimental data obtained through the height digital image correlation (*hDIC*) technique [46] satisfied the requirement for high-quality data with multiple components [47,48]. This approach allows the full-field mapping of residual stresses in discontinuously processed bodies manufactured by LPBF additive manufacturing [49] and welding [50]. However, the reliability of reconstructions with this approach depends on the quality and quantity of the experimental data. The error in reconstruction increases as the distance from the source of experimental data increases [45].

Diffraction techniques allow mapping residual elastic strains within a volume close to the surface or inside the volume in a pointwise fashion [51,52]. However, distinct measurements can only provide information about compatibility of strains or equilibrium of stresses if high spatial resolution is achieved. Tomography techniques that rely on Bragg edge diffraction data obtained using neutron [53–56] and X-ray diffraction [57,58] allow the reconstruction of continuous residual elastic strain maps [59–61]. The requirement of long scan times in the case of high density or thick metallic materials increases the cost of this type of experimentation and limits the application of this highly effective approach to two-dimensional mapping of residual elastic strains [62].

In the context of LPBF additive manufacturing with the CM 247 LC superalloy, this study aims to introduce an innovative methodology tailored for reconstructing residual stresses within large-scale parts characterized by a substantial height to data projection area ratio. This pioneering approach utilizes two-dimensional diffraction strain tomography data of residual elastic strains, coupled with eigenstrain reconstruction. By employing a minimum number of tomographic scans, this approach enables the complete volumetric characterization of all eigenstrain and residual stress components non-destructively, a capability not achievable through traditional non-destructive assessment methods. The minimization of tomography scans reduces experimentation costs, while a well-designed algorithm for voxel-based eigenstrain reconstruction [45] provides accurate maps of residuals. Relying on continuum mechanics, the method facilitates the calculation of three components of eigenstrains to reconstruct six components of residual stresses and residual elastic strains, along with three components of displacements within the domain. Applying the fundamental rules of continuum mechanics, this method not only ensures the satisfaction of compatibility conditions and equilibrium but also establishes a robust correlation with the experimental data integral to the reconstruction process, thereby enhancing its applicability and precision within the realm of high-tech industries.

In this study comprehensive assessment of eigenstrains and residual stresses formed as a consequence of the LPBF additive manufacturing of CM 247 LC superalloy parts is presented. Numerical experiments were conducted to investigate the influence of voxel spatial resolution and basis function parameters on the accuracy of the reconstruction in a domain that mimics discontinuous processing conditions of additive manufacturing parts. Further analyses were performed to determine the optimal number of data layers of diffraction strain tomography required to achieve full-scale reconstruction of residual stresses and eigenstrains. The robustness of the tomographic eigenstrain reconstruction of residual stresses in CM 247 LC superalloy is demonstrated by cross-referencing them with the experimental data used in the computations. Additionally, the effectiveness of this method in reconstructing residual stress components that diverge from the experimental data is validated through X-ray diffraction $\sin^2\psi$ and neutron diffraction residual stress quantifications. Complementary microstructure analysis is given to validate the reliability of eigenstrain distribution, taking into account its correlation with grain size and the distribution of residual stresses.

2. Methodology

The finite element solver employed for eigenstrain reconstruction was developed on the FEniCS computing platform. This study presents numerical analyses of mapping full-field residual stress distribution in large domains and the analysis of residual stresses in a CM 247 LC additive manufacturing part with discontinuous processing features using this solver. Numerical experiments were performed by creating artificial experimental data sets that mimic the planar distribution of the normal

component of residual elastic strains [62] reconstructed by the diffraction strain tomography technique [60]. Conducting experiments using this technique is expensive and requires high computational power for solving the linear elastic finite element solutions for each independent basis function. To reduce the overall cost of experimentation and computation, the parameters of eigenstrain reconstruction were analysed through four stages of numerical experiments. Results of eigenstrain reconstruction performed using highly reliable synchrotron diffraction data were validated by two different diffraction techniques.

2.1. Sample Preparation

This study presents the use of reliable experimental data acquired through diffraction strain tomography to reconstruct eigenstrain in additive manufacturing parts with unpredictable residual stress distribution that poses challenges in simplifying assumptions and formulating regularization functions. To meet these requirements, a large-scale CM 247 LC part was manufactured using the LPBF additive manufacturing technique. This method generates complex thermal effects at the nano- and micro-levels, resulting in intricate and unpredictable residual stress distribution.

This manufacturing process intentionally omitted predetermined parameters that could offer insights into the residual stress distribution. To ensure independence between specimen design and eigenstrain reconstruction, these two stages of the project were carried out in separate laboratories located at The University of Sheffield and The University of Oxford respectively. Fig. 1 displays the geometric dimensions of the printed rectangular part, with a Cartesian coordinate system originating from the midpoint of the part's bottom plane, and the image of CM 247 LC superalloy produced using additive manufacturing. In this study, a large-scale domain is determined to be a rectangular part with a hight that is larger than the dimensions of experimental data projection planes.

2.2. Tomographic eigenstrain reconstruction

Residual stresses are formed due to irregularly distributed permanent plastic strains, which eigenstrain theory refers to as eigenstrains [63,64]. The voxel-based methodology for eigenstrain reconstruction utilizes independent basis functions and experimental data to map the distribution of eigenstrains. This approach employs the principle of superposition, where the guiding information, such as displacements or residual elastic strains, is obtained either non-destructively or destructively. The resulting eigenstrain field is then imported into a numerical or analytical model, which establishes the relationship between eigenstrains and residual stresses, enabling the mapping of residual stresses. More information about the numerical model used for full-field eigenstrain reconstruction of residual stresses can be found in the paper introducing the voxel-based eigenstrain reconstruction method [45]. Eq. 1 presents a modified form of radial basis functions, which facilitates the distribution of independent eigenstrain components based on the Euclidean distance between the field point (x, y, z) and the voxel coordinates (x_l, y_l, z_l). The parameter r determines the localization range of the eigenstrain field.

$$F_l(x,y,z) = \left(\frac{1}{1 + \sqrt{(x-x_l)^2 + (y-y_l)^2 + (z-z_l)^2}} \right)^r \tag{1}$$

The FEniCS numerical model utilizes radial basis functions to compute six residual stress components. It relies on experimental data from a limited part region, which may exhibit the part's elastic response in terms of residual elastic strain or displacement. These responses arise from the material's elastic behaviour due to internal forces caused by irregular distribution of permanent plastic strains and changes in boundary conditions. The provided formulations for solving the inverse eigenstrain problem can handle both displacements and residual elastic strains as experimental data without requiring modifications. If experimental data is available from different part regions, their sequential implementation will suffice for performing least squares optimization, aiming to minimize the disparity between model-derived data based on radial basis functions and experimental data.

Numerical experiments were conducted to test this method's capability in reconstructing full-field residual stresses across large domains. The experiments utilized an artificially created part undergoing

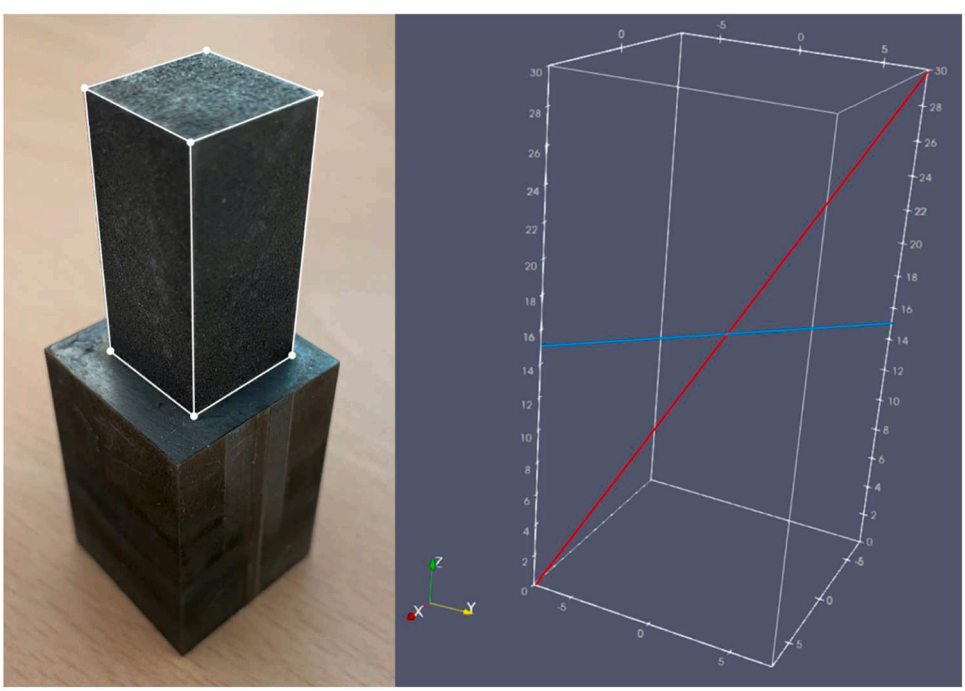

Fig. 1. Illustration of a CM 247 LC superalloy specimen produced by additive manufacturing, along with the corresponding domain with dimensions of 15.2 × 15.2 × 30.0 mm. The red and blue diagonal lines indicate the paths utilized for generating line plots.

discontinuous processing, which relies on eigenstrain distribution. Bodies with eigenstrain variation following a constant distribution normal to a plane are referred to as continuously processed bodies. If irregularities in permanent plastic strains are present along all three axes within a volume, these bodies are defined as parts undergoing discontinuous processing. For numerical investigations, a rectangular domain measuring 15.2 × 15.2 × 30.0 mm, that has the same geometric features with LPBF additive manufacturing specimen of CM 247 LC superalloy, was subjected to discontinuous processing artificially by achieving the distribution of eigenstrains using Eq. 2 given below.

$$\varepsilon^*_{ij}(x,y,z) = k_{ij} e^{(-ax)^2} e^{(-by)^2} (c-z)^{0.5} \tag{2}$$

In Eq. 2, x, y, and z represent the x-, y-, and z-coordinates, respectively. The magnitudes of the three components of eigenstrain were adjusted to match the dimensions of the part, utilizing the parameter k_{ij}. Specifically, for the xx-, yy-, and zz-components of eigenstrain, the values were set as 0.0667, 0.0667, and 0.0333, respectively, based on the geometric features of the rectangular domain as defined in Eq. 3. Constants a, b, and c are determined to be 0.2667, 0.2667, and 30.0, respectively, to achieve the eigenstrain distribution illustrated in Fig. 2. The selection of constants a and b relies on matching the eigenstrain distribution on the xy-plane of the numerical model domain to observations on the processes such as quenching. The choice of constant c is motivated by matching the eigenstrain distribution to the geometric position while ensuring that the chosen function $\sqrt{c-z}$ remains real-valued, i.e., $(c-z) > 0$. This formulation amplifies the magnitude of eigenstrains in the middle sections of the xy-plane, from top to bottom along the z-axis.

$$\varepsilon^*_{xx} = \varepsilon^*_{yy} = 2\varepsilon^*_{zz} \tag{3}$$

Fig. 2 illustrates the distribution of artificial eigenstrains and corresponding residual elastic strains in a domain consisting of 10 × 10 × 20 cells. These cells accommodate second-order Lagrange family Continuous Galerkin elements. The experimental data for residual elastic strains were collected from degrees of freedom points located at planes parallel to xy-plane. These planes were positioned with a fixed gap of 7.5 mm along the z-axis. This arrangement of experimental data represents the reference state conditions for numerical experimentation. The spacing between the data planes was adjusted to analyse the amount of experimental data required for eigenstrain reconstruction.

Diffraction strain tomography allows non-destructive and precise mapping of residual elastic strains. This technique's capability has significant potential for generating highly reliable experimental data required to comprehensively reconstruct residual stresses using full-field eigenstrain analysis. While neutron diffraction strain tomography shows promise in providing comparable data, synchrotron X-ray diffraction strain tomography [60] is chosen to demonstrate full-field eigenstrain reconstruction in large domains due to its prior validation [61] in accurately mapping residual elastic strains through planar techniques, as confirmed by numerical simulations. In this study, the experimental mapping of residual stresses utilizes a singular component of experimental data obtained through the synchrotron X-ray diffraction strain tomography technique, as detailed in the study conducted by Korsunsky et al. [62]. The filtered-back projection algorithm (iradon) within the MATLAB® programming platform was employed for this purpose. Investigations into various filtering options revealed no significant difference in the magnitude and distribution of the mapped residual elastic strains. Consequently, the filtering option for this algorithm was maintained at the default ramp filter setting.

Synchrotron X-ray diffraction experiments for X-ray diffraction strain tomography were carried out in ID15A beamline of ESRF in Grenoble France. For this experimentation, CM 247 LC superalloy additive manufacturing part was placed on a sample stage which had the capability of applying triaxial translation and rotation around the vertical z-axis. The monochromatic incident beam, that was collimated to the dimensions of 100 × 100 μm, provided 100 keV photon energy. Monochromatic beam with a size of $(h \times v)$ transmitted through the specimen along the gauge volume length $L(x, \varnothing)$ as illustrated in Fig. 11 and scattered to form diffraction cones to be collected by two-dimensional Perkin-Elmer large area detector. Calibration was accomplished using stress-free CeO_2 for the determination of exact value of the radiation energy and the sample detector distance. Scans were performed at five sampling volumes illustrated in Fig. 3(a, b) in a range of 180 degrees with a step size of 5 degree starting from zero degree. Scans for each rotation angle performed at 115 beam spots that covers a

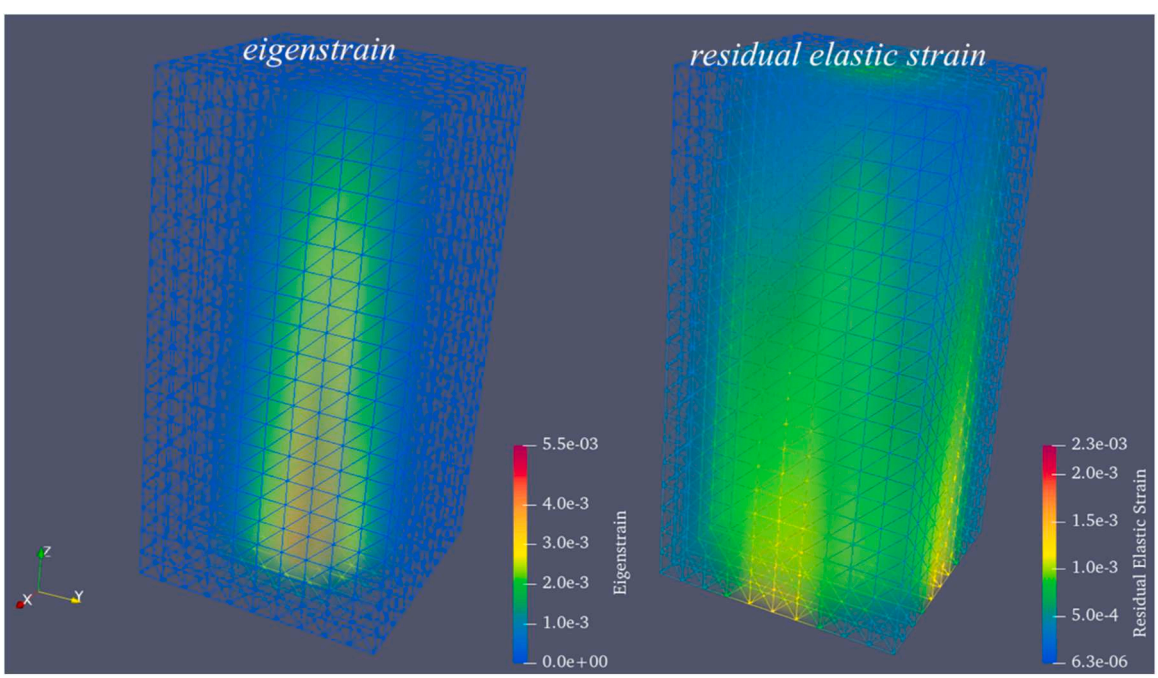

Fig. 2. The illustration of distribution of magnitudes of all components of eigenstrains (left) and residual elastic strains (right) within the domain of artificial discontinuous processing part created for numerical experiments.

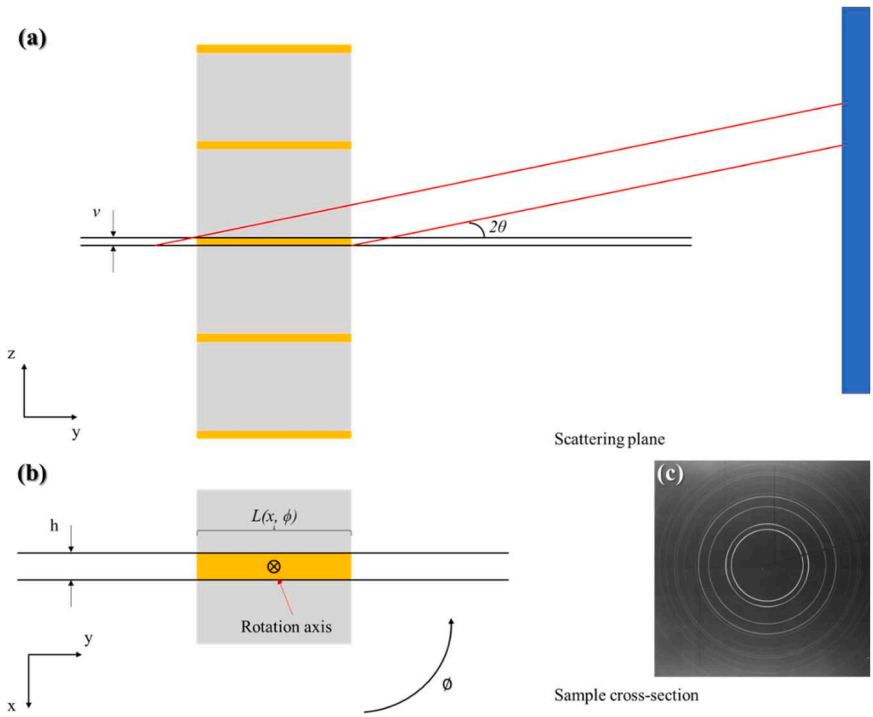

Fig. 3. (a) Illustration of the scattering geometry of the incident beam with a height of *v*, showing its transmission through five sampling volumes. (b) Cross-sectional representation of the diffraction experiment, depicting the beam width of *h*. (c) Illuminations in the form of Debye Scherrer rings.

translation range of 23.0 mm that is wider than the diagonal size of the specimen that is 21.5 mm. Illuminations in the form of Debye Scherrer rings, as shown in Fig. 3(c), on the detector as a result of Bragg diffraction by an angle of 2θ, as exemplified in Fig. 3(a), was used to deduce the apparent value of the lattice parameter corresponding to the z-axis within each gauge volume by Rietveld refinement characterisation technique using GSAS-II Crystallography Data Analysis Software.

2.3. Experimental validation

The X-ray diffraction $\sin^2\psi$ is a relatively simple and non-destructive technique that uses the interaction between X-ray beams and spacing between atomic planes in a crystal lattice according to the Bragg's Law [65] for the quantification of normal and shear components of residual elastic strains [66,67]. It is commonly employed to assess stresses in machined, heat-treated, or manufactured materials. This technique can also be used to measure residual stresses in additive manufacturing materials to distinguish the influence of printing parameters on the formation of residual stresses [68]. In this study, the validation of reconstructed residual stresses by an independent residual stress quantification technique was achieved using non-destructive X-ray diffraction $\sin^2\psi$ technique based on the formulation given by Korsunsky and Brandt [65] based on polar coordinates given in Fig. 4(a). The limitations of the experimental setup in Diamond Light Source B16 beamline, provided a limited portion of illuminations of diffraction data in the form of Debye Scherrer rings as illustrated in Fig. 4(b). This information was used for the determination of data centre and the application of the caking method within a range of 10 degree [57] using own code developed for this purpose. Measurements were conducted in a grid of 7 × 7 measurement points and averaged for each axis as illustrated in Fig. 4(c) and performed for *xx*- and *yy*-components of residuals individually.

Neutron diffraction strain scanning is a powerful and non-destructive crystallographic technique that harnesses the unique wave-like

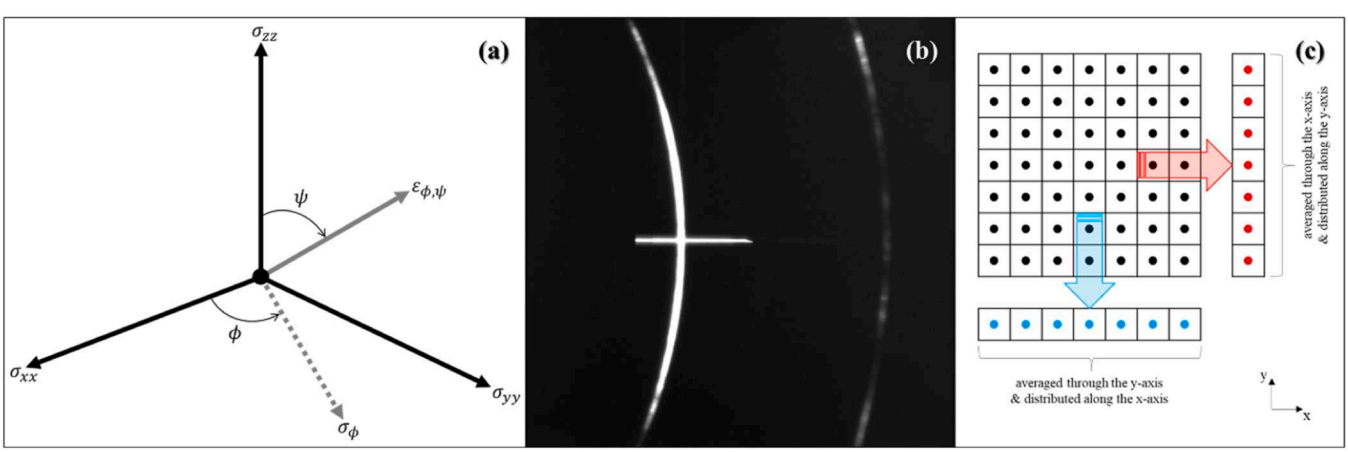

Fig. 4. (a) Coordinate system for the calculation of residual stresses using the X-ray diffraction $\sin^2\psi$ technique, (b) illuminations in the form of Debye Scherrer rings on the detector used for the calculations and (c) the measurement grid along with averaging paths for *xx*- and *yy*-components of residual stress.

properties of neutrons to reveal the atomic structure of materials. Neutrons, with their wavelengths closely matching atomic spacings, can penetrate deep into materials, making them the ideal probe for exploring the atomic intricacies of dense and thick substances. One remarkable application of this technique, pioneered by Allen et al. [69] in 1985, is neutron strain scanning, which assesses stress distribution within voluminous materials. By applying Bragg's law, it measures changes in inter-planar spacings of the crystalline lattice, allowing the inference of strain values by comparing stressed and unstressed samples. Neutron strain scanning's non-destructive nature, combined with its superior penetration depth when compared to X-rays, makes it invaluable for scrutinizing stress fields within materials, exemplified by its application to additive manufacturing specimen of CM 247 LC superalloy. This technique offers a comprehensive understanding of material stress fields, benefiting materials scientists and engineers seeking to characterize the macroscopic elastic strain tensor within various materials.

The analysis of the time-of-flight neutron strain scanning data was carried out using the Open Genie software of ISIS ENGIN-X beamline. The peak positions in the time-of-flight (TOF) diffraction spectrum were ascertained through a least-squares refinement process, and Bragg's law was utilized to derive the inter-planar spacing. The fundamental reflections {220}, {200}, {111}, and {311}, illustrated in Fig. 5, were specifically employed for strain analysis, as they encompass relevant information concerning both the γ and γ' phases, following the same approach explained in the previous study [26]. Measurements were conducted from 15 sampling points within a gauge volume of $2 \times 2 \times 2$ mm along the diagonal path illustrated in Fig. 5, with the sampling volume positioned at the centre along the build direction (z-axis). The xx- and yy-components of residual elastic strains were quantified, as illustrated in Fig. 5, with detectors situated parallel to the diagonal normal to the measurement path. The reference pattern of reflections for the Bragg's law calculations was determined to be the average of four measurements obtained from the two edges of the diagonal path.

3. Results

Efficient and cost-effective residual stress analyses are considered

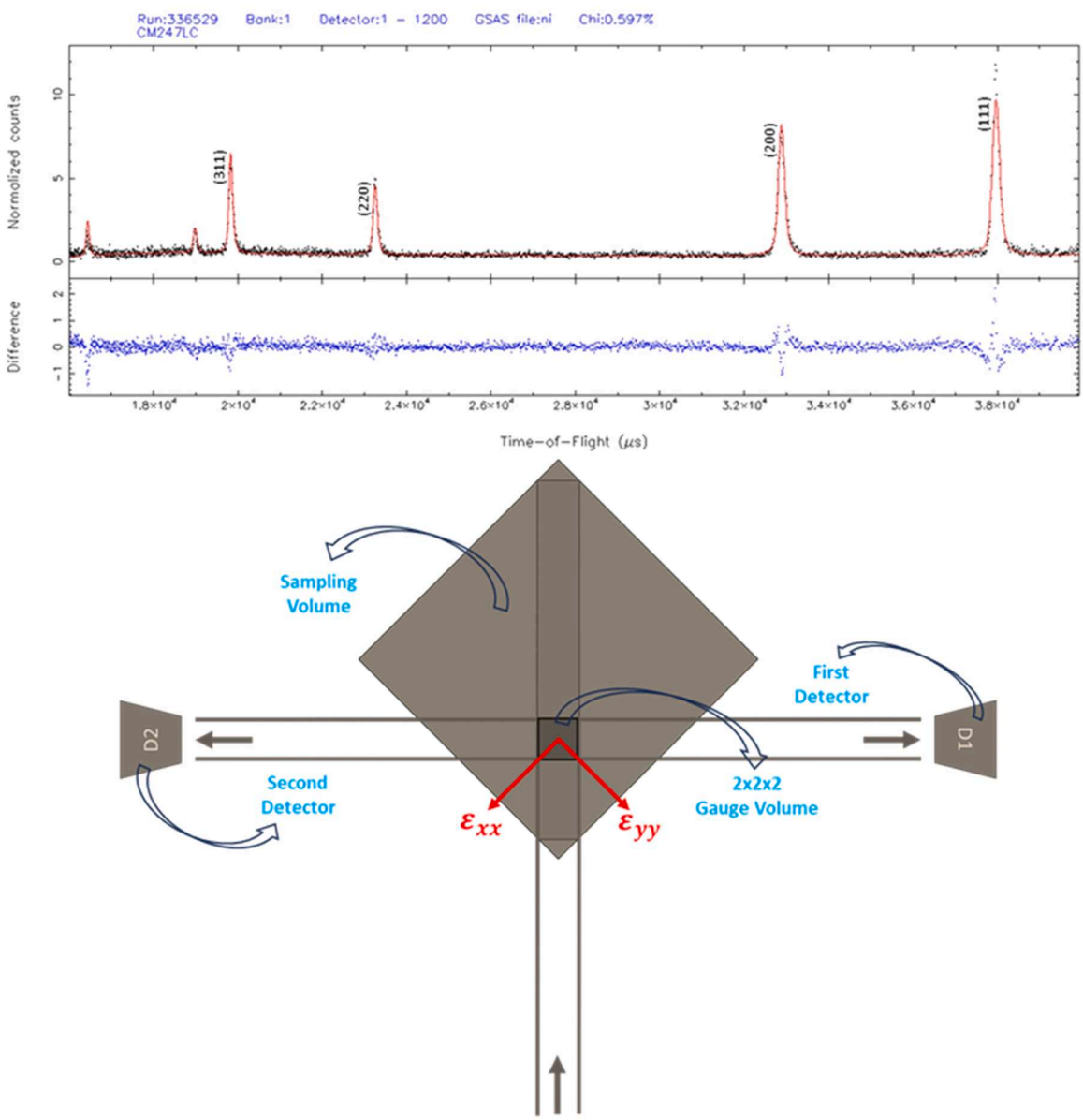

Fig. 5. Time-of-flight diffraction spectrum of CM 247 LC superalloy in the reference condition, acquired using the Open Genie Software at ISIS ENGIN-X, alongside a schematic diagram of neutron strain scanning via time-of-flight measurements.

paramount, especially for additive manufacturing parts utilized in high-tech industries such as aerospace. Various parameters of the voxel-based eigenstrain reconstruction method, including voxel density, radial basis function parameters, and the quantity of experimental data, were systematically analysed to satisfy this requirement. After each test, model variables were adjusted, and subsequent analyses were conducted while keeping the corresponding variable constant. These investigations provided valuable insights into the potential accuracy of full-field residual stress reconstruction, particularly when the diffraction strain tomography technique is the source of experimental data. Validations achieved using highly reliable diffraction techniques demonstrated the capability of tomographic eigenstrain reconstruction in determining all components of residual stresses in the case of limited experimental data with a single component.

3.1. Numerical experiments on voxel density

The analysis on voxel density was completed by dividing the rectangular domain into cubic cells arranged in multiples of $1 \times 1 \times 2$ cells, starting from $4 \times 4 \times 8$ cells up to $20 \times 20 \times 40$ cells, and performing eigenstrain reconstruction with the radial basis function parameter set to 10,000. Each cell accommodates 12 s-order Lagrange family Continuous Galerkin elements. Each solution was accomplished by the creation of an artificial part undergoing discontinuous processing and solving the inverse problem of eigenstrain [64]. Reconstructions were performed using three components of experimental data to calculate three components of eigenstrain and nine components of residual elastic strain. To assess deviation from the reference state, the reconstructed eigenstrain and residual elastic strain distributions were compared with magnitudes in an artificial domain. The objective is to reconstruct all normal components of eigenstrains alongside the normal and shear components of residual elastic strains. Thus, the root mean squared error and mean calculations encompass all corresponding components. The analysis results demonstrate that increasing cell density reduces reconstruction errors. However, there is a point of saturation after which further improvement becomes indiscernible. This saturation is observed when the total number of cells reaches 2000, arranged in a $10 \times 10 \times 20$ grid as depicted in Fig. 6. Subsequent analyses were performed while maintaining this cell arrangement.

3.2. Numerical experiments on radial basis function parameter

The radial basis function defined in Eq. 1 ranges from a unit function that sets the center of the voxel to 1 while keeping the rest of the field points at 0, to a constant function that sets all points, including the center of the voxel, to 1 by addressing the function parameter r from zero to positive infinity. This variation is analyzed by ranging the function parameter from 10,000 to 0.1 in independent solutions using 5 layers of experimental data distributed in a domain composed of 2000 cells arranged in a $10 \times 10 \times 20$ grid. Error analysis was conducted as explained in the cell density analysis. Similar to the previous analysis, reconstructions were carried out using three components of experimental data to calculate three components of eigenstrain and nine components of residual elastic strain.

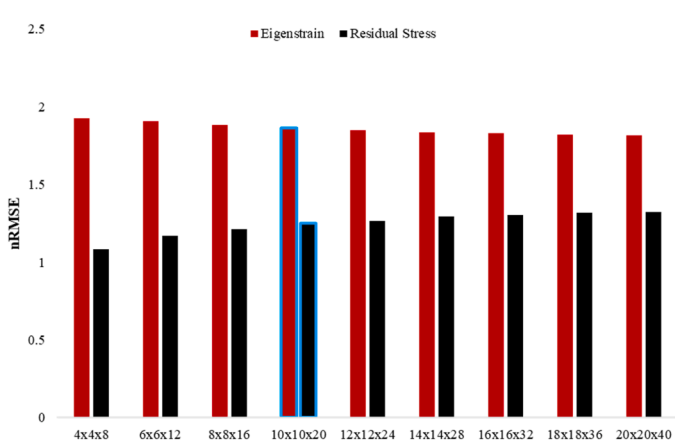

Fig. 6. Comparison of normalised Root Mean Squared Errors (nRMSE) of reconstructed eigenstrain and residual elastic strain components w.r.t the mean of reference state eigenstrain and residual elastic strain components, considering variations in cell density.

Results presented in Fig. 7 indicate that the function exhibits constant function behaviour when the parameter value is 6 or higher. The reconstruction quality improves for both eigenstrain and residual elastic strain as the parameter value decreases, reaching its peak at 0.6. Further reduction in the parameter value continues to decrease the error in the reconstruction of residual elastic strains; however, it leads to a significant deterioration of eigenstrain values when compared to the reference state, as the function behaves more like a continuous function. After reaching a parameter value of 0.4, the errors in eigenstrain reconstruction become exceptionally high, resulting in the exclusion of results for parameter values of 0.3, 0.2 and 0.1. Subsequent analyses were carried out by setting the function parameter to 0.6 while maintaining the previously determined cell arrangement.

3.3. Numerical experiments on experimental data components

The diffraction strain tomography technique provides a planar distribution of residual elastic strain components normal to the projected plane. Consequently, the analysis, which assumes the ideal condition of having three normal components of experimental data, is revised to only require the availability of the normal-to-data-plane component, specifically the zz-component of residual elastic strains. Fig. 8 presents the planar distribution of eigenstrain magnitudes and the zz-component of residual elastic strain in both the reference and reconstructed states, considering the availability of the zz-component of experimental data only. These diagonal planes pass through the origin and are parallel to the z-axis. The results demonstrate that the zz-component of residual elastic strain can be reconstructed accurately using the zz-component of experimental data and previously determined model parameters. The quality of the reconstructed residual elastic strain in these plots is exceptional. Although the overall distribution of eigenstrains is highly reliable even without any guiding function, it does not reach the level of accuracy achieved in the reconstruction of residual elastic strain.

Fig. 9 illustrates the distribution of the zz-component of eigenstrains and residual elastic strains. It is evident that the reconstructed eigenstrains and residual elastic strains perfectly match the reference state when the experimental data components from five layers are available. Therefore, it can be concluded that both eigenstrains and residual elastic strains can be reconstructed with highly reliable quality when only a single component of experimental data is available.

3.4. Numerical experiments on experimental data quantity

The analysis of experimental data components revealed the potential for highly reliable reconstruction of eigenstrain and residual elastic strains. This can be achieved by utilizing a single data component perpendicular to the data planes. To minimize computational and experimental costs while accurately mapping residual elastic strains, further investigation focused on determining the optimal quantity of experimental data needed for significantly low reconstruction error. Four distinct data layer configurations, as illustrated in Fig. 10, were investigated throughout the domain. Initially, the domain comprises two data layers at the top and bottom. The arrangement of layers was then altered by consecutively inserting a new layer between every pair of planes.

The results presented in Fig. 11 indicate that the inclusion of additional data layers beyond the 5-layer arrangement does not lead to any

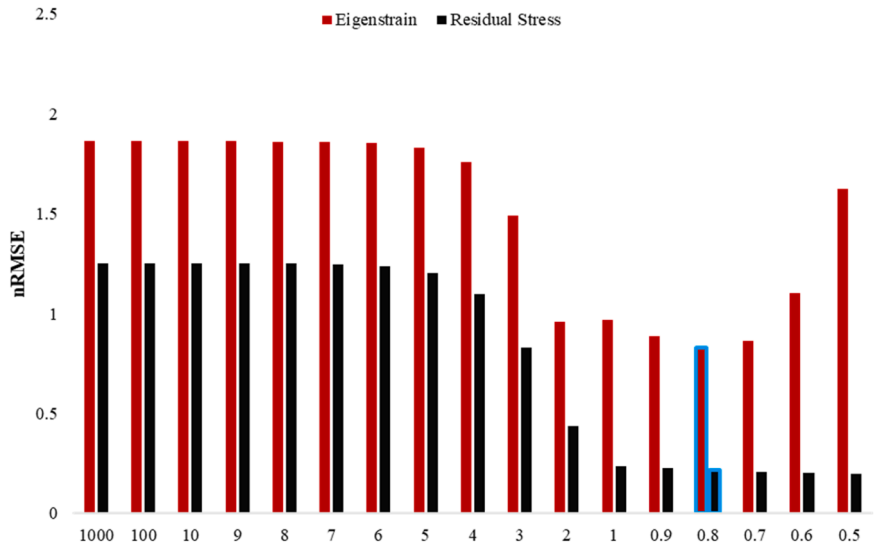

Fig. 7. Comparison of normalised Root Mean Squared Errors (nRMSE) of reconstructed eigenstrain and residual elastic strain components w.r.t the mean of reference state eigenstrain and residual elastic strain components, considering different radial basis function parameters.

improvement when using a single component of experimental data for reconstruction. It is important to note that alternative arrangements of experimental data, such as those with 4, 6, or 8 layers evenly distributed at a constant axial distance, did not yield better results. In fact, resulting in higher reconstruction errors compared to the 3-, 5-, and 9-layer solutions and causing deviations in the correlation between data layers and reconstruction error. Consequently, the most effective approach for distributing data layers in diffraction strain tomography and quantification of residual elastic strains involves including central planes between the primary planes (initially at the top and bottom) and increasing the number of layers gradually.

Further analysis by diagonal line plots given in Fig. 12 reveals the overlapping characteristics of reconstructed eigenstrains and residual elastic strains between the 5- and 9-layer configurations. This suggests that accurate reconstruction is achieved in terms of both eigenstrains and residual elastic strains by utilizing 5 layers of experimental data that contains information about one component of elastic deformation. Moreover, the line plots of eigenstrains demonstrate that the presented method enables the mapping of permanent plastic strains responsible for the formation of residual elastic strains and residual stresses within a physical part in the case of availability of high-quality experimental data that can be obtained using diffraction strain tomography techniques.

Results also show that reliable results can also be obtained with 2- and 3-layer configurations although the 5-layer arrangement is optimal. The analysis results for data layers given in Fig. 12 indicate the potential to obtain highly accurate information on residual elastic strain within two-thirds of the domain. This can be achieved by using only two layers of experimental data from the top and bottom sections for reconstruction. However, in the middle section, noticeable deviations in residual elastic strains from the reference condition emerge after reconstructing with such data. As the reconstruction error decreases towards the data layers, as seen in Fig. 12, the results from a 3-layer arrangement of experimental data show an excellent match between reconstructed residual elastic strains and the reference state when compared to 2 layers solution. Additionally, this arrangement provides a reliable reconstruction of eigenstrains, closely resembling the reference condition. Therefore, considering the reliance on costly diffraction measurements in diffraction strain tomography, the number of data layers can be reduced to three from five for a cost-effective analysis of residual elastic strains.

3.5. Analysis of additive manufacturing CM 247 LC part

The processed dataset was utilized to map two-dimensional distribution of the *zz*-component of residual elastic strains. This was achieved using the Radon transform mathematical framework, based on principles explained in Korsunsky et al.'s study [62]. As mentioned in that study, geometric effects resulting from the sample position relative to the rotation axis and its shape must be considered when quantifying lattice spacing. To correct systematic errors of this nature, the deviation of the rotation axis from the cross-section centre of gravity was quantified by summing integral values of experimental data from the reference angle at zero degrees. However, accurate information about the gauge volume length is required to determine these integral values. In this study, such information was extracted from the two-dimensional map of lattice spacing values, which varied with angle and scan position, by determining the local standard deviation. The peak values of the local standard deviation were observed at the edges of the specimen positioned along the scan axis. By retaining the data points corresponding to the peak standard deviation values, a contour map of the average lattice parameter variation with projection number was obtained as illustrated in Fig. 13(a). After determining the path length at each angle, the parameters necessary for error correction were calculated. The sinogram, obtained by mapping the integral values of lattice spacing onto a *x*-∅ grid, served as the input for the filtered back projection algorithm, allowing the mapping of lattice spacing distribution on the cross-sectional plane. Residual elastic strains corresponding to each lattice spacing value at each plane were quantified using stress-free lattice spacing value. The stress-free lattice spacing value was estimated as the average of all lattice spacing values determined from five planes. The strains were subsequently mapped for each plane, similar to the one shown in Fig. 13(b), which corresponds to the middle plane. The distribution of residual elastic strains appears to be erratic, but this is not attributable to noise. The highly variable distribution is an outcome of the chaotic nature of the LPBF additive manufacturing process. Since the primary objective of the study is the comprehensive reconstruction of all residual stress details, the experimental data and planar distributions obtained using the strain tomography technique were not subjected to further processing for regularization.

The *zz*-component of eigenstrains and residual stresses, reconstructed using 5 layers of experimental data, are displayed in Fig. 14. The distribution of reconstructed residual stresses is found to be consistent with strain tomography reconstructions, thereby providing

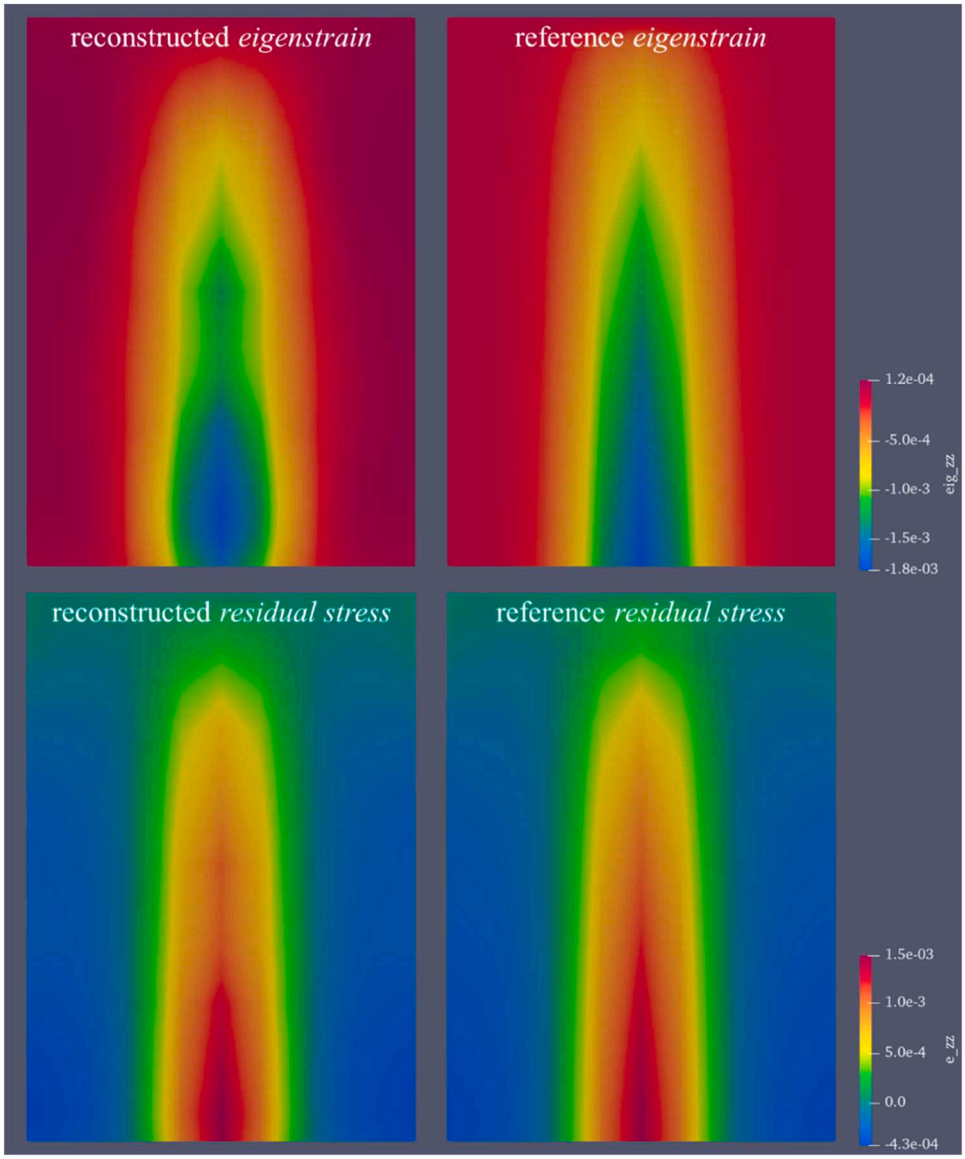

Fig. 8. The distribution of reference (right) and reconstructed (left) states of *zz*-component of eigenstrain (top) and *zz*-component of residual elastic strains (bottom) in the diagonal plane that is parallel to the z-axis and passes from the origin.

validation for the reliability of the *zz*-component of residual stresses and residual elastic strains. As expected, residual stresses resulting from the chaotic nature of non-uniform heating and cooling cycles in LPBF additive manufacturing are found to exist in a compressive form in the central region, while tension predominates in the outer layers. Commencing from the central section of the part, compressive residual stresses are divided into two branches by tension along the build direction (*z*-axis), forming a conical configuration. This novel observation highlights the capability of the presented tomographic eigenstrain reconstruction method in revealing hidden features of residual stresses. The lower section of the part exhibits a blurred distribution of residual stresses, with a mixed combination of tension and compression. This indeterminate behaviour is attributed to the challenges of collecting X-ray diffraction data at the boundary between the printed part and the build platform. While further processing may rectify such errors, it also risks losing important details. Consequently, this minor deviation is not considered in the analysis. Consistency in the distribution of eigenstrains is observed in relation to residual stresses. Along the build direction (*z*-axis), the *zz*-component of eigenstrains exhibits a non-linear increase in magnitude. The non-uniform distribution of eigenstrains is attributed to the formation of residual stresses. A U-shaped hot spot is present in the eigenstrains, which parallels the branched pattern of residual stresses, much like the distribution of the latter. The branched distribution of residual stresses and eigenstrains is a result of the complex interplay between the manufacturing process, directional factors, and the effectiveness of the data collection and reconstruction methods. Understanding and characterizing these distributions are essential for optimizing the performance and reliability of additive manufacturing parts.

The line plots in Fig. 15 demonstrate that the distribution of eigenstrains is strongly influenced by the number of experimental data layers. Similar distributions with varying magnitudes are exhibited by eigenstrains using 3 and 5 layers of experimental data, mirroring the findings of numerical experiments. Conversely, a perfect match of 3- and 5-layer solutions is observed in the distribution of residual stresses, consistent with the results of the numerical experiments presented in Figs. 11 and 12. The characteristic distribution of residual stresses parallel to the building direction in the additive manufacturing part of CM 247 LC superalloy with a rectangular shape is also illustrated by these line plots, aligning along the red diagonal line in Fig. 1. Additionally, these results

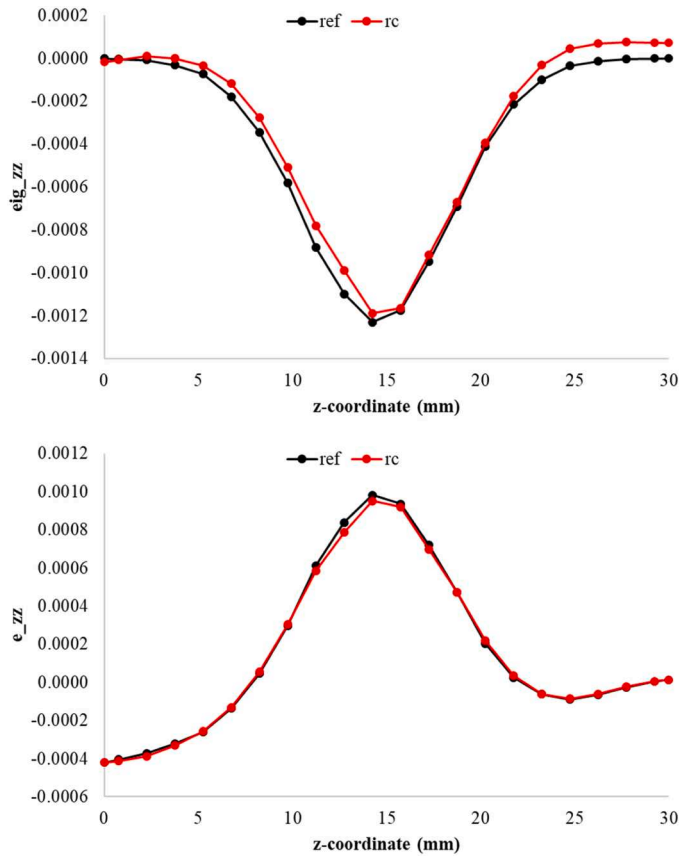

Fig. 9. The distribution of *zz*-component of eigenstrains (*eig_zz*) and residual elastic strains (*e_zz*) along the red line depicted in Fig. 1 in the reference (*ref*) and reconstructed (*rc*) conditions.

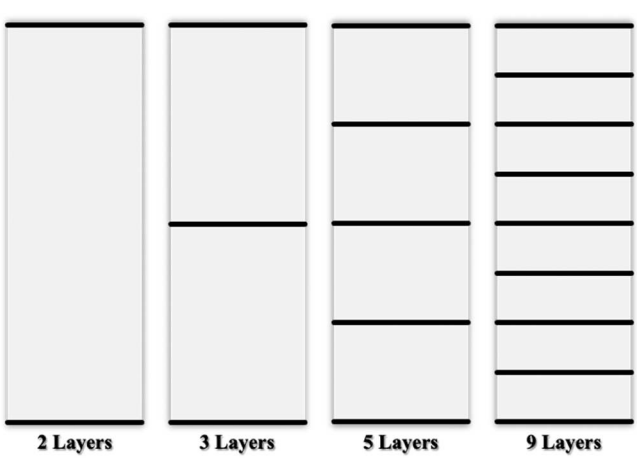

Fig. 10. Data layer arrangement obtained by dividing the gap between two layers into two sections, starting from the initial configuration of top and bottom layers.

reveal a comprehensive understanding of the transition of residual stress from tensile to compressive along the diagonal, covering all sections of the additive manufacturing part. In the case of eigenstrains, the magnitude of variations in the distribution leads to the formation of residual stresses. Line plots of eigenstrains show similar variations, despite having different magnitudes. Accordingly, the similarity in variation demonstrates the reliability of reconstruction using a lower amount of experimental data. This achievement is significant as it reduces the cost of experimentation.

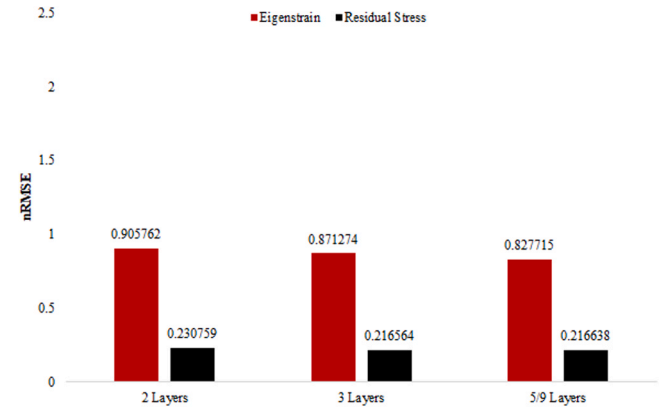

Fig. 11. Comparison of normalised Root Mean Squared Errors (nRMSE) of reconstructed eigenstrain and residual elastic strain components w.r.t the mean of reference state eigenstrain and residual elastic strain components, considering the number of layers.

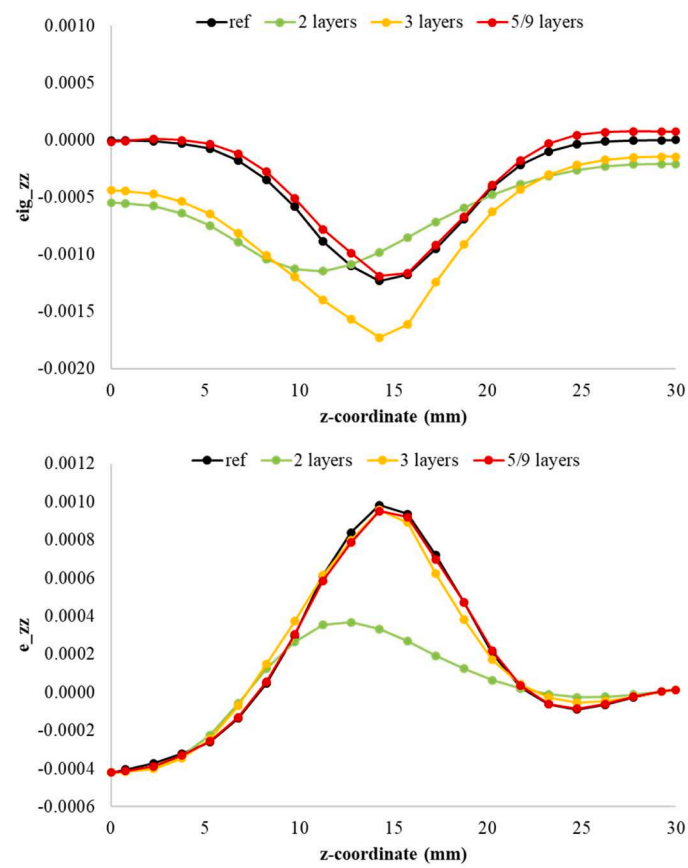

Fig. 12. The distribution of *zz*-component of eigenstrains (*eig_zz*) and residual elastic strains (*e_zz*) along the red line shown in Fig. 1. The distribution of the 9-layer solution is founded to completely overlap with the 5-layer solution.

Eigenstrain reconstruction based on strain tomography data projections provides inherent validation for the reconstruction of the *zz*-component of residual stresses that are parallel to experimental data component. This validation specifically applies to the *z*-component of the experimental data, which is parallel to the build direction of additive manufacturing and quantified using monochromatic X-ray diffraction beams. To assess the quality of reconstruction for the components of residual stresses other than the component of experimental data, X-ray diffraction $\sin^2\psi$ measurements and neutron diffraction strain scanning

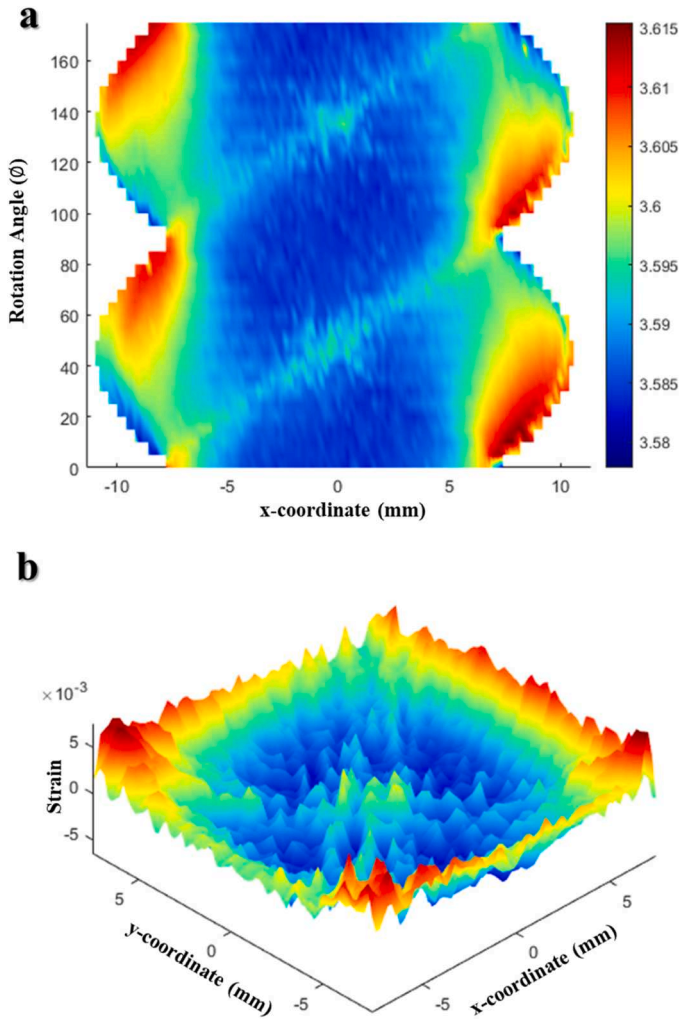

Fig. 13. (a) Distribution of average lattice parameters projected onto the grid of translation range with respect to rotation angle and (b) residual elastic strains mapped by diffraction strain tomography projected to the centre plane, which is located at the middle height of the additive manufacturing part.

were conducted at the midplane of the additive manufacturing part illustrated in Fig. 3(a) for the quantification of *xx*- and *yy*-components of residual elastic strains. Subsequent to the determination of residual elastic strains, residual stresses were calculated based on plane stress assumption [70]. Fig. 16 depicts the distribution of *xx*- and *yy*-components of residual stresses which do not align with the experimental data.

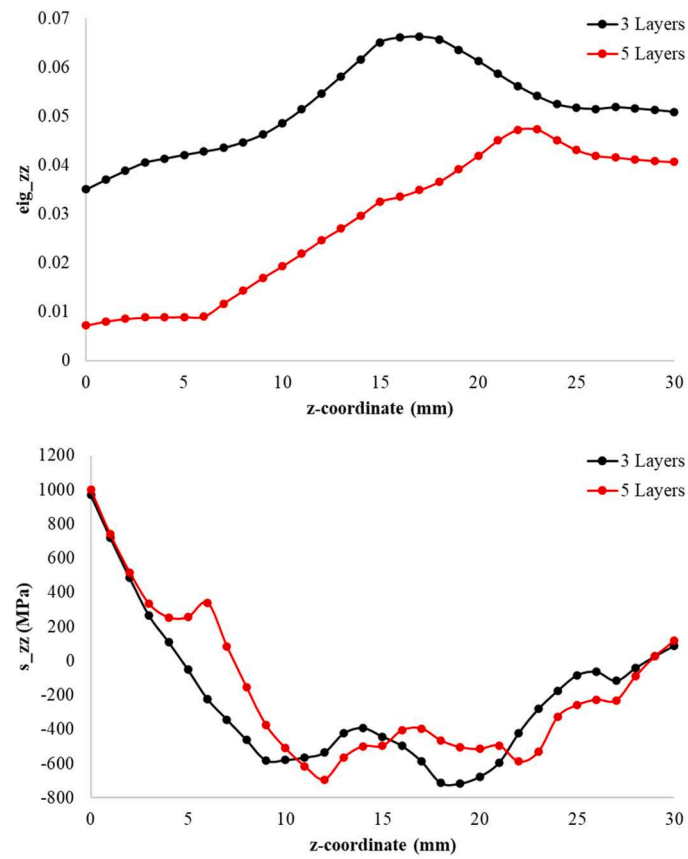

Fig. 15. Line plots showing the distribution of the *zz*-component of eigenstrains (*eig_zz*) and residual stresses (*s_zz*), along the volume diagonal depicted as red line in Fig. 1, that were reconstructed using 3 and 5 layers of experimental data.

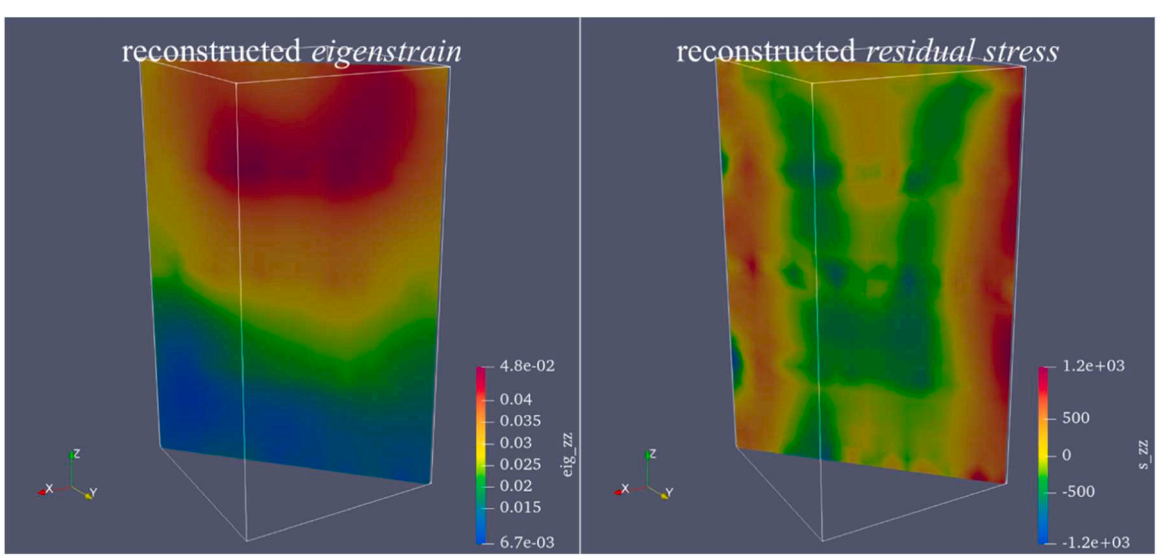

Fig. 14. The distribution of *zz*-component of eigenstrains (*eig_zz*) and residual stresses (*s_zz*) along the volume diagonal reconstructed using 5 layers of experimental data obtained from X-ray diffraction strain tomography.

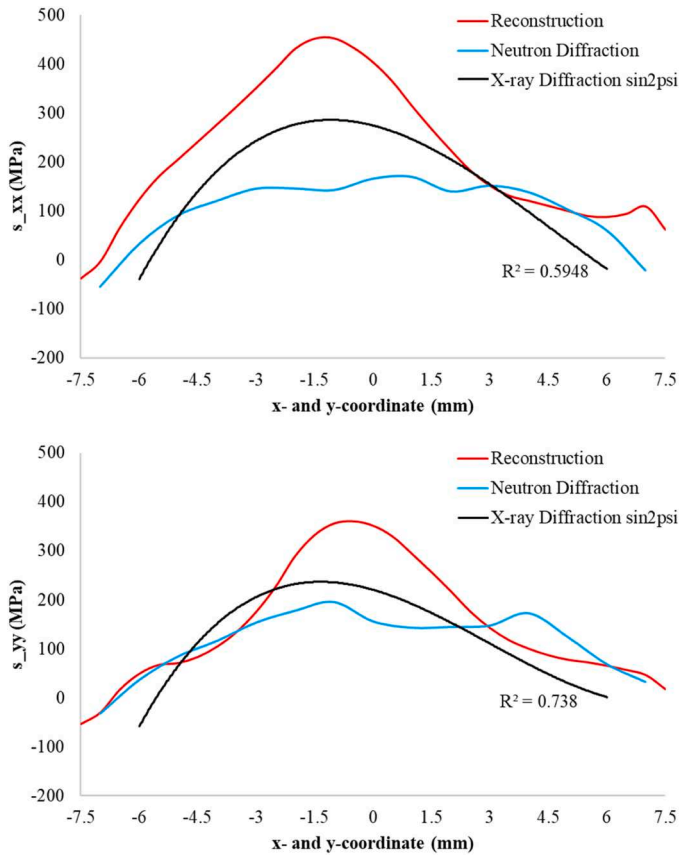

Fig. 16. Line plots showing the distribution of *xx*- and *yy*-components of residual stresses that were quantified by tomographic eigenstrain reconstruction, neutron diffraction and X-ray diffraction $\sin^2\psi$ (sin2psi).

In this plot, eigenstrain reconstruction and neutron diffraction values distribute along the blue diagonal line at the middle plane parallel to the plane of powder bed (*xy*-plane) as shown in Fig. 1. On the other hand, X-ray diffraction $\sin^2\psi$ quantifications distribute along y- and x-axes for *xx*- and *yy*-components of residual stresses respectively. Neutron diffraction quantification corresponds to lattice spacing calculations with a maximum uncertainty less than 0.01% while X-ray diffraction $\sin^2\psi$ quantifications provide least squared fitting of measurements over the grid given in Fig. 4(c) with the coefficients of determination of 0.5958 and 0.738 for *xx*- and *yy*-components of residual stresses respectively.

Comparing the quantifications obtained from two experimental techniques with the results of the reconstruction performed using 5 layers of experimental data, a highly reliable match in the distribution of both residual stress components is observed. It is worth noting that the magnitude of both components of the X-ray diffraction quantifications deviates from the other components, which can be attributed to errors arising during experimentation and difference of distribution paths. This significant deviation of magnitudes does not affect the fact that the distribution of reconstruction results matches with the X-ray diffraction quantifications. On the other hand, the uncertainty of neutron diffraction quantifications less than 0.01% proves high reliability of this residual elastic strain quantification technique. The expectation is that the calculations of tomographic eigenstrain approach is able to provide residual stresses magnitudes similar to the ones observed in neutron diffraction quantifications in the case of availability of experimental data components parallel to the plane of powder bed (*xy*-plane).

During the LPBF additive manufacturing of CM 247 LC parts, heterogeneous nucleation is expected to initiate grain formation at the solid steel substrate and molten liquid metal interface. This is because the complex rapid heating and cooling cycles of this process require longer time scales for homogeneous nucleation to occur. The resulting grains elongate along the building direction (*z*-axis) while having an equiaxed form parallel to the plane of powder bed (*xy*-plane). Accordingly, grain size among the other microstructural properties like crystallographic defects, crystallographic texture, and precipitates of additive manufacturing parts [71] have an important role on understanding the distribution of permanent plastic strains. This characteristic form of grains in LPBF manufactured CM 247 LC parts was analysed using electron backscattered diffraction (EBSD) images as illustrated in Fig. 17. Microstructure maps obtained from the vicinity of strain tomography data projections located at the top, middle, and bottom of the specimen show that the grains grow along the building direction. These results demonstrate that the CM 247 LC specimen exhibits a microstructure that supports the reliability of its production.

Microstructure of the top and bottom regions have similar visual properties that is smaller grains elongate parallel to the build direction (*z*-axis) while microstructure in the middle region accommodates larger grains. In combination with the residual stress and eigenstrain distributions given in Fig. 15, a relation between microstructure grain size and *zz*-component of eigenstrains and residual stresses, that is smaller grain sizes tend to result in higher levels of residual stress, is observed. According to Hall-Petch effect [72,73], larger grains are more likely to be deformed plastically than smaller grains. Eigenstrain and residual stress quantifications given in this study are consistent with that fact by presenting higher magnitude of eigenstrains in the middle region where grains are larger and higher magnitude of residual stresses in smaller grain regions due to irregular distribution of eigenstrains. This study's quantification of eigenstrain and residual forces does not explicitly address grain size or strength. Residual stress is intricately linked to internal geometrically necessary dislocations within the microstructure, among other contributing factors. In the realm of continuum mechanics, plastic deformations can solely be defined through numerical quantification. Consequently, the results correlating grain size with yield strength are presented to validate the model calculations.

4. Conclusion

Residual stress analysis is an essential requirement in engineering parts crafted from CM 247 LC and other superalloys using additive manufacturing techniques, ensuring the structural integrity and performance reliability of these parts in the demanding and high-stress environments encountered during the utilizations of high-tech industries such as aerospace. This study presents the tomographic reconstruction of three components of eigenstrains, six components of residual elastic strains, six components of residual stresses, and three components of displacements comprehensively using a numerical experimentation approach and the analysis of residual stresses in a CM 247 LC additive manufacturing part validated by employing independent X-ray and neutron diffraction residual stress quantifications along with microstructural analysis.

The results of the numerical analysis demonstrate that a perfect reconstruction is possible in terms of residual elastic strains and corresponding residual stresses. However, achieving a perfect match of eigenstrains, so called inherent strains or permanent plastic strains, should not be expected in real case applications because of experimental errors. The reconstructed eigenstrains in numerical experiments show a highly excellent match in terms of distribution, albeit with a slight shift in magnitudes observed. In the context of continuum mechanics, identifying irregularities in the distribution of eigenstrain is crucial, and these results, with their highly reliable distribution, fulfil this requirement. Although real quantities may differ, this variation appears as a total shift rather than irregular deviations. Since this resulting total shift does not impact the final residual elastic strains, it can be concluded that the presented approach provides reliable information about the distribution of eigenstrains, which are permanent plastic strains that induce

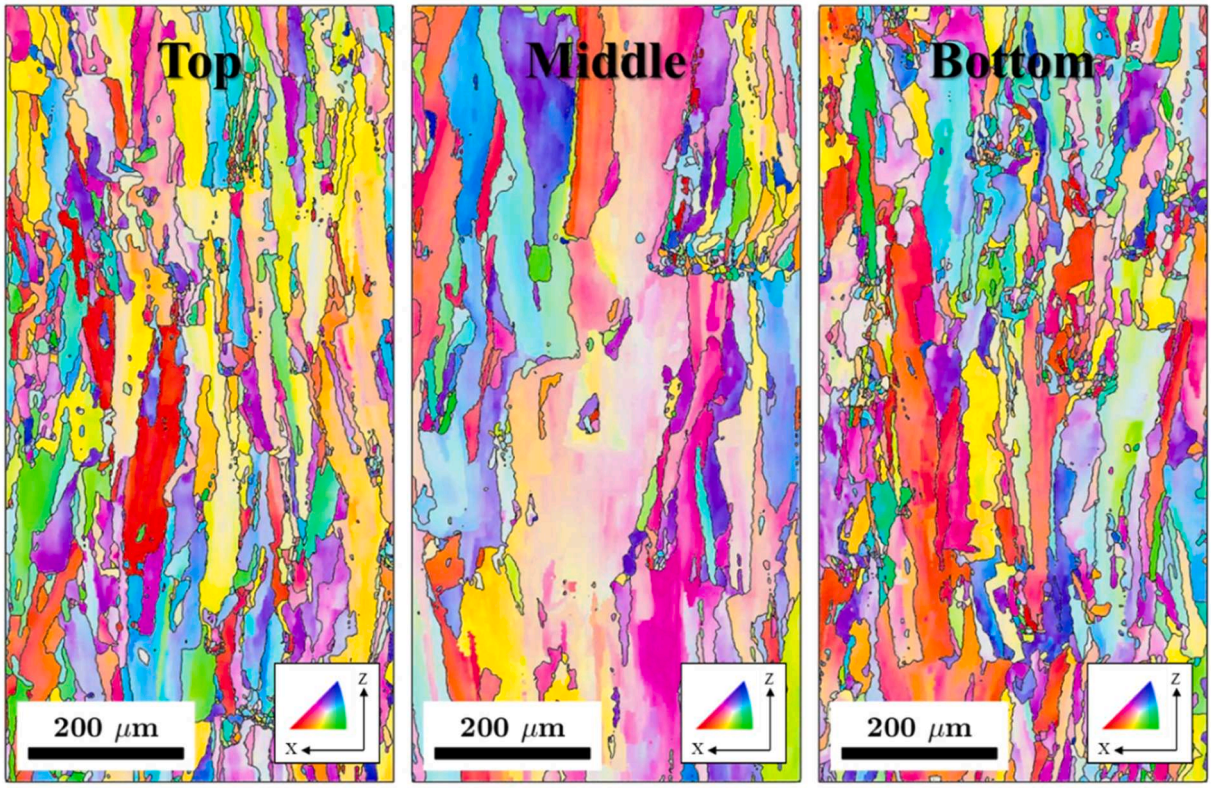

Fig. 17. EBSD images showing elongated grains on the side surface of the CM 247 LC specimen, captured in the vicinity of strain tomography data projections at the top, middle, and bottom.

the formation of residual stresses.

Additional guiding information regarding the magnitude of eigenstrains can enhance the model's performance. Nonetheless, the aim of tomographic eigenstrain reconstruction is to eliminate the requirement for guiding information and regularization functions in extensive volumes. This investigation illustrated that as the problem grows more intricate, with an increasing height to data projection area ratio, cost-effective reconstruction of residual stresses can be achieved. However, enhancing the quality and quantity of data is crucial for achieving a more accurate eigenstrain distribution. Consequently, future studies should concentrate on improving data collection techniques to enhance the reconstruction quality of both eigenstrains and residual stresses.

Eigenstrains and residual stresses obtained from the analysis of additive manufacturing specimens are expected to have a quality similar to numerical experiments. However, it's important to note that the accuracy of quantification depends on the reliability of the experimental data. By employing highly dependable diffraction tomography for projecting residual elastic strain, it is assumed that this error can be minimized. The analysis results also confirm the characteristic distribution of eigenstrains and residual stresses in additive manufacturing specimens along the volume diagonal, a finding supported by microstructure analysis. In summary, the study's findings demonstrate the feasibility of mapping all components of residual stress within a discontinuously processed part using a limited amount of experimental data.

CRediT authorship contribution statement

Uzun Fatih: Writing – review & editing, Writing – original draft, Visualization, Validation, Software, Resources, Methodology, Investigation, Funding acquisition, Formal analysis, Data curation, Conceptualization. **Basoalto Hector:** Investigation. **Korsunsky Alexander M.:** Supervision, Project administration, Methodology, Funding acquisition, Conceptualization. **Chen Jingwei:** Investigation. **Dolbnya Igor P.:** Investigation. **Besnard Cyril:** Investigation. **Wang Zifan Ivan:** Investigation. **Slim Mohamed Fares:** Investigation. **Lee Tung Lik:** Investigation. **Liogas Konstantinos:** Investigation.

Declaration of Competing Interest

The authors declare that they have no known competing financial interests or personal relationships that could have appeared to influence the work reported in this paper.

Data Availability

Data will be made available on request.

Acknowledgements

The authors acknowledge EuroHPC project grant EHPC-DEV-2022D10-054 for allowing the simulations to be performed on the Luxembourg national supercomputer MeluXina and are also grateful to LuxProvide teams for their expert support. The authors thank Diamond Light Source (Didcot, UK) for beamtime allocation MM30460-1 to B16 beamline and European Synchrotron Radiation Facility (Grenoble, France) for beamline allocation MA5208 to ID15A beamline. The authors also thank ISIS Neutron and Muon Source (Didcot, U.K.) for beamline allocation to ENGIN-X Beamline.

References

[1] R.J. Smith, G.J. Lewis, D.H. Yates, Development and application of nickel alloys in aerospace engineering, Aircr. Eng. Aerosp. Technol. 73 (2001) 138–146, https://doi.org/10.1108/00022660110694995.
[2] M. Valenti, Building more efficient turbines, Mech. Eng. 116 (1994) 52–56.
[3] W. Danesi, R. Thielemann, Nickel Base Alloy (1970) 3720509.

[4] J.H. Boswell, D. Clark, W. Li, M.M. Attallah, Cracking during thermal post-processing of laser powder bed fabricated CM247LC Ni-superalloy, Mater. Des. 174 (2019) 107793, https://doi.org/10.1016/j.matdes.2019.107793.

[5] S. Sanchez, P. Smith, Z. Xu, G. Gaspard, C.J. Hyde, W.W. Wits, I.A. Ashcroft, H. Chen, A.T. Clare, Powder Bed Fusion of nickel-based superalloys: a review, Int J. Mach. Tools Manuf. 165 (2021), https://doi.org/10.1016/j.ijmachtools.2021.103729.

[6] R.S.K. Harris, G. Erickson, MAR M 247 Derivations - CM 247 LC DS Alloy and CMSX Single Crystal Alloys: Properties & Performance, in: J.F.R. M. Gell, C. S. Kortovich, R. H. Bricknell, W. B. Kent (Ed.), Fifth International Symposium on Superalloys, The Metallurgical Society of AIME, Champion, Pennsylvania, USA, 1984: pp. 221–230. https://doi.org/10.7449/1984/SUPERALLOYS_1984_221_230.

[7] G.L. Erickson, K. Harris, R.E. Schwer, Directionally Solidified DS CM 247 LC - Optimized Mechanical Properties Resulting From Extensive γ′ Solutioning, in: Proceedings of the ASME 1985 International Gas Turbine Conference and Exhibit. Volume 4: Manufacturing Materials and Metallurgy; Ceramics; Structures and Dynamics; Controls, Diagnostics and Instrumentation; Education; Process Industries, ASME, Houston, Texas, USA, 1985. https://doi.org/10.1115/85-GT-107.

[8] A. Seidel, T. Finaske, A. Straubel, H. Wendrock, T. Maiwald, M. Riede, E. Lopez, F. Brueckner, C. Leyens, Additive manufacturing of powdery Ni-based superalloys Mar-M-247 and CM 247 LC in hybrid laser metal deposition, Met. Mater. Trans. A Phys. Met. Mater. Sci. 49 (2018) 3812–3830, https://doi.org/10.1007/s11661-018-4777-y.

[9] M.B. Henderson, D. Arrell, M. Heobel, R. Larsson, G. Marchant, Nickel-based superalloy welding practices for industrial gas turbine applications, Sci. Technol. Weld. Join. 9 (1) (2004) 14, https://doi.org/10.1179/136217104225017099.

[10] R. Engeli, T. Etter, S. Hövel, K. Wegener, Processability of different IN738LC powder batches by selective laser melting, J. Mater. Process Technol. 229 (2016) 484–491, https://doi.org/10.1016/j.jmatprotec.2015.09.046.

[11] D.D. Gu, W. Meiners, K. Wissenbach, R. Poprawe, Laser additive manufacturing of metallic components: materials, processes and mechanisms, Int. Mater. Rev. 57 (2012) 133–164, https://doi.org/10.1179/1743280411Y.0000000014.

[12] L.N. Carter, M.M. Attallah, R.C. Reed, Laser powder bed fabrication of nickel-base superalloys: Influence of parameters; characterisation, quantification and mitigation of cracking, Proc. Int. Symp. Superalloys (2012) 577–586, https://doi.org/10.7449/2012/superalloys_2012_577_586.

[13] S. Catchpole-Smith, N. Aboulkhair, L. Parry, C. Tuck, I.A. Ashcroft, A. Clare, Fractal scan strategies for selective laser melting of 'unweldable' nickel superalloys, Addit. Manuf. 15 (2017) 113–122, https://doi.org/10.1016/j.addma.2017.02.002.

[14] A. Alhuzaim, S. Imbrogno, M.M. Attallah, Direct laser deposition of crack-free CM247LC thin walls: mechanical properties and microstructural effects of heat treatment, Mater. Des. 211 (2021) 110123, https://doi.org/10.1016/J.MATDES.2021.110123.

[15] M. Cloots, P.J. Uggowitzer, K. Wegener, Investigations on the microstructure and crack formation of IN738LC samples processed by selective laser melting using Gaussian and doughnut profiles, Mater. Des. 89 (2016) 770–784, https://doi.org/10.1016/j.matdes.2015.10.027.

[16] H. Wang, L. Chen, B. Dovgyy, W. Xu, A. Sha, X. Li, H. Tang, Y. Liu, H. Wu, M. S. Pham, Micro-cracking, microstructure and mechanical properties of Hastelloy-X alloy printed by laser powder bed fusion: as-built, annealed and hot-isostatic pressed, Addit. Manuf. 39 (2021) 101853, https://doi.org/10.1016/j.addma.2021.101853.

[17] M.J. Donachie, S.J. Donachie, Superalloys: A Technical Guide, in: 2002.

[18] O.A. Ojo, N.L. Richards, M.C. Chaturvedi, Contribution of constitutional liquation of gamma prime precipitate to weld HAZ cracking of cast Inconel 738 superalloy, Scr. Mater. 50 (2004) 641–646, https://doi.org/10.1016/j.scriptamat.2003.11.025.

[19] T. Lehmann, D. Rose, E. Ranjbar, M. Ghasri-khouzani, M. Tavakoli, H. Henein, T. Wolfe, A.J. Qureshi, T. Lehmann, D. Rose, E. Ranjbar, M. Ghasri-khouzani, Large-scale metal additive manufacturing, a Holist. Rev. State Art. Chall. (2022), https://doi.org/10.1080/09506608.2021.1971427.

[20] M.F. Zaeh, G. Branner, Investigations on residual stresses and deformations in selective laser melting, Prod. Eng. 4 (2010) 35–45, https://doi.org/10.1007/s11740-009-0192-y.

[21] F. Uzun, A.N. Bilge, Ultrasonic investigation of the effect of carbon content in carbon steels on bulk residual stress, J. Nondestr Eval. 34 (2015) 11, https://doi.org/10.1007/s10921-015-0284-x.

[22] M.R. Hill, M.D. Olson, A.T. DeWald, Biaxial residual stress mapping for a dissimilar metal welded nozzle, J. Press. Vessel Technol., Trans. ASME 138 (2016) 1–9, https://doi.org/10.1115/1.4031504.

[23] E.S. Statnik, F. Uzun, S.A. Lipovskikh, Y.V. Kan, S.I. Eleonsky, V.S. Pisarev, P.A. Somov, A.I. Salimon, Y.V. Malakhova, A.G. Seferyan, D.K. Ryabov, A.M. Korsunsky, Comparative Multi-Modal, Multi-Scale Residual Stress Evaluation in SLM 3D-Printed Al-Si-Mg Alloy (RS-300) Parts, Metals 2021, Vol. 11, Page 2064 11 (2021) 2064. https://doi.org/10.3390/MET11122064.

[24] H. Soyama, A.M. Korsunsky, A critical comparative review of cavitation peening and other surface peening methods, J. Mater. Process. Tech. 305 (2022) 117586, https://doi.org/10.1016/j.jmatprotec.2022.117586.

[25] F. Uzun, A.N. Bilge, Immersion ultrasonic technique for investigation of total welding residual stress, Procedia Eng. 10 (2011) 3098–3103, https://doi.org/10.1016/j.proeng.2011.04.513.

[26] F. Uzun, C. Papadaki, Z. Wang, A.M. Korsunsky, Neutron strain scanning for experimental validation of the artificial intelligence based eigenstrain contour method, Mech. Mater. 143 (2020) 103316, https://doi.org/10.1016/j.mechmat.2020.103316.

[27] L.E. Lindgren, Finite element modeling and simulation of welding part 1: increased complexity, J. Therm. Stress. 24 (2001) 141–192, https://doi.org/10.1080/01495730150500442.

[28] L.E. Lindgren, Finite element modeling and simulation of welding part 2: improved material modeling, J. Therm. Stress. 24 (2001) 195–231, https://doi.org/10.1080/014957301300006380.

[29] L.E. Lindgren, Finite element modeling and simulation of welding. Part 3: efficiency and integration, J. Therm. Stress. 24 (2001) 305–334, https://doi.org/10.1080/01495730151078117.

[30] P.J. Bouchard, The NeT bead-on-plate benchmark for weld residual stress simulation, Int. J. Press. Vessels Pip. 86 (2009) 31–42, https://doi.org/10.1016/j.ijpvp.2008.11.019.

[31] M.C. Smith, A.C. Smith, NeT bead-on-plate round robin: comparison of transient thermal predictions and measurements, Int. J. Press. Vessels Pip. 86 (2009) 96–109, https://doi.org/10.1016/j.ijpvp.2008.11.016.

[32] F. Hosseinzadeh, J. Kowal, P.J. Bouchard, Towards good practice guidelines for the contour method of residual stress measurement, J. Eng. (2014), https://doi.org/10.1049/joe.2014.0134.

[33] J. Everaerts, E. Salvati, F. Uzun, L. Romano Brandt, H. Zhang, A.M. Korsunsky, Separating macro- (Type I) and micro- (Type II+III) residual stresses by ring-core FIB-DIC milling and eigenstrain modelling of a plastically bent titanium alloy bar, Acta Mater. 156 (2018) 43–51, https://doi.org/10.1016/j.actamat.2018.06.035.

[34] F. Uzun, J. Everaerts, L.R. Brandt, M. Kartal, E. Salvati, A.M. Korsunsky, The inclusion of short-transverse displacements in the eigenstrain reconstruction of residual stress and distortion in in740h weldments, J. Manuf. Process 36 (2018) 601–612, https://doi.org/10.1016/j.jmapro.2018.10.047.

[35] B. Zhu, N. Leung, W. Kockelmann, M. Gorley, M.J. Whiting, Y. Wang, T. Sui, Neutron Bragg edge tomography characterisation of residual strain in a laser-welded Eurofer97 joint, Nucl. Mater. Energy 36 (2023) 101462, https://doi.org/10.1016/j.nme.2023.101462.

[36] C. Zhao, N.D. Parab, X. Li, K. Fezzaa, W. Tan, A.D. Rollett, T. Sun, Critical instability at moving keyhole tip generates porosity in laser melting, 1979, Science 370 (2020) 1080–1086, https://doi.org/10.1126/science.abd1587.

[37] Y. Wang, W. Guo, Y. Xie, H. Li, C. Zeng, M. Xu, H. Zhang, In-situ monitoring plume, spattering behavior and revealing their relationship with melt flow in laser powder bed fusion of nickel-based superalloy, J. Mater. Sci. Technol. 177 (2024) 44–58, https://doi.org/10.1016/j.jmst.2023.07.068.

[38] M.B. Prime, Cross-sectional mapping of residual stresses by measuring the surface contour after a cut, J. Eng. Mater. Technol. 123 (2001) 162, https://doi.org/10.1115/1.1345526.

[39] M. Turski, L. Edwards, Residual stress measurement of a 316l stainless steel bead-on-plate specimen utilising the contour method, Int. J. Press. Vessels Pip. 86 (2009) 126–131, https://doi.org/10.1016/j.ijpvp.2008.11.020.

[40] A.T. DeWald, M.R. Hill, Multi-axial contour method for mapping residual stresses in continuously processed bodies, Exp. Mech. 46 (2006) 473–490, https://doi.org/10.1007/s11340-006-8446-5.

[41] M.E. Kartal, Y.H. Kang, A.M. Korsunsky, A.C.F.F. Cocks, J.P. Bouchard, The influence of welding procedure and plate geometry on residual stresses in thick components, Int J. Solids Struct. 80 (2016) 420–429, https://doi.org/10.1016/j.ijsolstr.2015.10.001.

[42] F. Uzun, A.M. Korsunsky, On the identification of eigenstrain sources of welding residual stress in bead-on-plate inconel 740H specimens, Int J. Mech. Sci. 145 (2018) 231–245, https://doi.org/10.1016/j.ijmecsci.2018.07.007.

[43] F. Uzun, A.M. Korsunsky, On the application of principles of artificial intelligence for eigenstrain reconstruction of volumetric residual stresses in non uniform Inconel alloy 740H weldments, Finite Elem. Anal. Des. 155 (2019) 43–51, https://doi.org/10.1016/j.finel.2018.11.004.

[44] F. Uzun, A.M. Korsunsky, On the analysis of post weld heat treatment residual stress relaxation in Inconel alloy 740H by combining the principles of artificial intelligence with the eigenstrain theory, Mater. Sci. Eng. A 752 (2019) 180–191, https://doi.org/10.1016/j.finel.2018.11.004.

[45] F. Uzun, A.M. Korsunsky, Voxel-based full-field eigenstrain reconstruction of residual stresses, Adv. Eng. Mater. (2023), https://doi.org/10.1002/adem.202201502.

[46] F. Uzun, A.M. Korsunsky, The height digital image correlation (hDIC) technique for the identification of triaxial surface deformations, Int J. Mech. Sci. 159 (2019) 417–423, https://doi.org/10.1016/j.ijmecsci.2019.06.014.

[47] F. Uzun, A.I. Salimon, E.S. Statnik, C. Besnard, J. Chen, T. Moxham, E. Salvati, Z. Wang, A.M. Korsunsky, Polar transformation of 2D X-ray diffraction patterns and the experimental validation of the hDIC technique, Measurement 151 (2019) 107193, https://doi.org/10.1016/j.measurement.2019.107193.

[48] F. Uzun, A.M. Korsunsky, The use of surface topography for the identification of discontinuous displacements due to cracks, Metals 10 (2020) 1–13, https://doi.org/10.3390/met10081037.

[49] F. Uzun, H. Basoalto, K. Liogas, J. Chen, I.P. Dolbnya, Z. Ivan, A.M. Korsunsky, Voxel-based full-field eigenstrain reconstruction of residual stresses in additive manufacturing parts using height digital image correlation, Addit. Manuf. 77 (2023) 103822, https://doi.org/10.1016/j.addma.2023.103822.

[50] F. Uzun, T.L. Lee, Z.I. Wang, A.M. Korsunsky, I. Neutron, M. Source, S. Rutherford, H. Campus, Full-field eigenstrain reconstruction for the investigation of residual stresses in finite length weldments, J. Mater. Process. Tech. 325 (2024) 118295, https://doi.org/10.1016/j.jmatprotec.2024.118295.

[51] C. Ohms, R.C. Wimpory, D.E. Katsareas, A.G. Youtsos, NET TG1: Residual stress assessment by neutron diffraction and finite element modeling on a single bead weld on a steel plate, Int. J. Press. Vessels Pip. 86 (2009) 63–72, https://doi.org/10.1016/j.ijpvp.2008.11.009.

[52] M.C. Smith, A.C. Smith, C. Ohms, R.C. Wimpory, The NeT Task Group 4 residual stress measurement and analysis round robin T on a three-pass slot-welded plate specimen, Int. J. Press. Vessels Pip. 164 (2018) 3–21, https://doi.org/10.1016/j.ijpvp.2017.09.003.
[53] J.R. Santisteban, L. Edwards, M.E. Fitzpatrick, A. Steuwer, P.J. Withers, M. R. Daymond, M.W. Johnson, N. Rhodes, E.M. Schooneveld, Strain imaging by Bragg edge neutron transmission, Nucl. Instrum. Methods Phys. Res A 481 (2002) 765–768, https://doi.org/10.1016/S0168-9002(01)01256-6.
[54] S. Pratihar, M. Turski, L. Edwards, P.J. Bouchard, Neutron diffraction residual stress measurements in a 316L stainless steel bead-on-plate weld specimen, Int. J. Press. Vessels Pip. 86 (2009) 13–19, https://doi.org/10.1016/j.ijpvp.2008.11.010.
[55] R.C. Wimpory, C. Ohms, M. Hofmann, R. Schneider, A.G. Youtsos, Statistical analysis of residual stress determinations using neutron diffraction, Int. J. Press. Vessels Pip. 86 (2009) 48–62, https://doi.org/10.1016/j.ijpvp.2008.11.003.
[56] B. Zhu, N. Leung, W. Kockelmann, S. Kabra, A.J. London, M. Gorley, M.J. Whiting, Y. Wang, T. Sui, Revealing the residual stress distribution in laser welded Eurofer97 steel by neutron diffraction and Bragg edge imaging, J. Mater. Sci. Technol. 114 (2022) 249–260, https://doi.org/10.1016/j.jmst.2021.12.004.
[57] A.M. Korsunsky, K.E. Wells, P.J. Withers, Mapping two-dimensional state of strain using synchroton X-ray diffraction, Scr. Mater. 39 (1998) 1705–1712, https://doi.org/10.1016/S1359-6462(98)00385-6.
[58] P.J. Withers, M. Preuss, P.J. Webster, D.J. Hughes, A.M. Korsunsky, Residual strain measurement by synchrotron diffraction, Mater. Sci. Forum 404–407 (2002) 1–12, https://doi.org/10.4028/www.scientific.net/msf.404-407.1.
[59] B. Abbey, S.Y. Zhang, W.J.J. Vorster, A.M. Korsunsky, Feasibility study of neutron strain tomography, Procedia Eng. 1 (2009) 185–188, https://doi.org/10.1016/j.proeng.2009.06.043.
[60] A.M. Korsunsky, W.J.J. Vorster, S.Y. Zhang, D. Dini, D. Latham, M. Golshan, J. Liu, Y. Kyriakoglou, M.J. Walsh, The principle of strain reconstruction tomography: Determination of quench strain distribution from diffraction measurements, Acta Mater. 54 (2006) 2101–2108, https://doi.org/10.1016/j.actamat.2006.01.003.
[61] J.N. Hendriks, C. Jidling, T.B. Schön, A. Wills, C.M. Wensrich, E.H. Kisi, Neutron transmission strain tomography for non-constant stress-free lattice spacing, Nucl. Instrum. Methods Phys. Res B 456 (2019) 64–73, https://doi.org/10.1016/j.nimb.2019.07.005.
[62] A.M. Korsunsky, N. Baimpas, X. Song, J. Belnoue, F. Hofmann, B. Abbey, M. Xie, J. Andrieux, T. Buslaps, T.K. Neo, Strain tomography of polycrystalline zirconia dental prostheses by synchrotron X-ray diffraction, Acta Mater. 59 (2011) 2501–2513, https://doi.org/10.1016/j.actamat.2010.12.054.
[63] T. Mura, Mechanics of elastic and inelastic solids, (1982). https://doi.org/10.1007/978–94-009–3489-4.
[64] A.M. Korsunsky, A Teaching Essay on Residual Stresses and Eigenstrains, Butterworth-Heinemann, Oxford, United Kingdom, 2017.
[65] A.M. Korsunsky, L.R. Brandt, The Effect of Deposition Parameters on the Mechanical and Transport Properties in Nanostructured Cu/W Multilayer Coatings, in: Functional Thin Films Technology, CRC Press, 2021: pp. 287–318.
[66] H.H. Lester, R.H. Aborn, Behaviour under stress of iron crystal in steel, Army Ordnance 6 (1925) 120–127.
[67] A.M. Korsunsky, A critical discussion of the sin2 ψ stress measurement technique, Mater. Sci. Forum 571–572 (2008) 219–224, https://doi.org/10.4028/www.scientific.net/msf.571-572.219.
[68] J. Čapek, E. Polatidis, N. Casati, R. Pederson, C. Lyphout, M. Strobl, Influence of laser powder bed fusion scanning pattern on residual stress and microstructure of alloy 718, Mater Des 221 (2022). https://doi.org/10.1016/j.matdes.2022.110983.
[69] A.J. Allen, M.T. Hutchings, C.G. Windsor, C. Andreani, Neutron diffraction methods for the study of residual stress fields, Adv. Phys. 34 (1985) 445–473, https://doi.org/10.1080/00018738500101791.
[70] A.J.G. Lunt, E. Salvati, L. Ma, I.P. Dolbyna, T.K. Neo, A.M. Korsunsky, Full in-plane strain tensor analysis using the microscale ring-core FIB milling and DIC approach, J. Mech. Phys. Solids 94 (2016) 47–67, https://doi.org/10.1016/j.jmps.2016.03.013.
[71] K.A. Liogas, K.B. Lau, Z. Wang, D.N. Brown, E. Polatidis, P. Wang, A.M. Korsunsky, Effect of heat treatment on the microstructure and magnetic properties of laser powder bed fusion processed equiatomic Co-Fe, Addit. Manuf. 67 (2023) 103499, https://doi.org/10.1016/j.addma.2023.103499.
[72] E.O. Hall, The deformation and ageing of mild steel: III discussion of results, Proc. Phys. Soc. Sect. B 64 (1951) 747–753, https://doi.org/10.1088/0370-1301/64/9/303.
[73] P.N. J, The cleavage strength of polycrystals, J. Iron Steel Inst. 174 (1953) 25–28.